Compare Mechanistic Predictions for Doped UO$_2$ Mechanical Response and Other Properties with Empirical Models and Experimental Measurements

September 2023

Technical Report

Ryan Sweet[1], Daniel J. vanWasshenova[1], Daniel Schwen[1], and Aysenur Toptan[1]

[1]Idaho National Laboratory

Idaho National Laboratory

Compare Mechanistic Predictions for Doped UO$_2$ Mechanical Response and Other Properties with Empirical Models and Experimental Measurements

Technical Report

Ryan Sweet[1], Daniel J. vanWasshenova[1], Daniel Schwen[1], and Aysenur Toptan[1]

[1]Idaho National Laboratory

September 2023

Idaho National Laboratory
Computational Mechanics and Materials Department
Idaho Falls, Idaho 83415

http://www.inl.gov

Page intentionally left blank

ABSTRACT

The U.S. Department of Energy's Nuclear Energy Advanced Modeling and Simulation program develops predictive capabilities using computational methods for the analysis and design of advanced reactor and fuel cycle systems. This program has been supporting the development of BISON, a high-fidelity, high-resolution fuel performance tool at the engineering scale. As part of its development, additional modeling capabilities and improvements have been developed for relevant fuel forms. In this work, a fuel creep deformation model for Cr-doped fuel has been implemented into BISON, along with improvements to the empirical UO_2 fuel creep model based on experimental data and improvements to the radial power factor calculation for doped fuels. This work allows for more accurate simulation analyses for both UO_2 and doped-UO_2 fuels.

DECLARATION OF COMPETING INTEREST

The authors declare that they have no known competing financial interests or personal relationships that could appear to have influenced the work reported in this technical report.

ORCID

Ryan Sweet   0000-0002-7919-4623
Daniel vanWasshenova   0000-0002-7224-777X
Daniel Schwen   0000-0002-8958-4748
Aysenur Toptan   0000-0003-4250-6336

CONTENTS

ACRONYMS

ANN	artificial neural network
DOE	U.S. Department of Energy
GPU	graphics processing unit
INL	Idaho National Laboratory
LANL	Los Alamos National Laboratory
LWR	light-water reactor
MOOSE	Multiphysics Object-Oriented Simulation Environment
NEAMS	Nuclear Energy Advanced Modeling and Simulation
RMSE	root-mean-square error
RMS	root-mean-square
ROM	reduced-order model
RPF	radial power factor

I. INTRODUCTION

This report presents results of the ongoing Nuclear Energy Advanced Modeling and Simulation (NEAMS) effort to more accurately model industry-relevant fuel concepts. In particular, this work focuses on implementing additional thermomechanical models for UO_2 and doped-UO_2 fuels.

This manuscript is organized into three distinct efforts targeting two different behaviors. Firstly, the radial power profile, which calculates the fuel power and subsequently fuel burnup distributions radially across the fuel, was modified to include additional cross sections for gadolinia, a popular burnable poison used in boiling-water reactor fuels. This effort also supported critical infrastructure improvements that made the results of this calculation more accurate across all supported fuel types.

The second behavior explored in this manuscript is based on the creep deformation of the fuel. At high temperatures, stresses, and fission rates, ceramic fuels experience significant deformation which reduces the material strength and increases the material compliance. This behavior is a fundamental aspect of fuel mechanical behavior and is critical for assessing fuel-cladding mechanical interaction in light-water reactors (LWRs). Two different approaches were taken for two different fuel materials. The fuel creep model used for UO_2, the MATRPO creep model, was re-investigated based on the presence of a newer and more comprehensive creep data set. This model was then sequentially refit to applicable data to generate new model coefficients and an improved UO_2 creep model. Data from a mechanistic model was used to generate a reduced-order model (ROM) for Cr-doped UO_2. This ROM was implemented into BISON for testing.

II. BURNUP CALCULATIONS

A necessary and significant refactoring and rebuilding of the methods used in calculating the burnup and RPF for UO_2 fuel was performed. The methods used within the **BurnupFunction** class follow the technique developed by Soba et al. (Soba et al., 2013, 2014; Soba and Denis, 2017). This section includes an in-depth recount of the motivations and implementations of this refactoring.

A. Finite Difference Higher Order Calculations

The **BurnupFunction** was designed to reflect the burnup, isotope concentration, and RPF on a secondary grid overlaid on the mesh. To allow for refinement near areas of interest within the fuel, this secondary grid has the ability to be refined or biased radially while retaining uniform spacing axially. Using Taylor series expansions at uneven grid spacing points, discrete finite-difference formulas for approximating first and second derivatives are used following the work of Liu et al. (1995).

Coefficients of the Finite-Difference Schemes	
First Derivative $(C_x)_i = \alpha_i^{\|} C_{i-2} + \beta_i^{\|} C_{i-1} - \left(\alpha_i^{\|} + \beta_i^{\|} + \gamma_i^{\|} \right) C_i + \gamma_i^{\|} C_{i+1} + \epsilon_i^{\|}$	(I.1)
One-point upstream scheme $\alpha_i^{\|} = 0 \quad \beta_i^{\|} = -1/d_{i-1} \quad \gamma_i^{\|} = 0$	(I.2)
Higher order scheme $\begin{cases} \alpha_i^{\|} &= d_{i-1}d_{i+1}/\left[d_{i-2}\left(d_{i-2}+d_{i+1}\right)\left(d_{i-2}-d_{i-1}\right)\right] \\ \beta_i^{\|} &= -d_{i-2}d_{i+1}/\left[d_{i-1}\left(d_{i-2}\left(d_{i-2}-d_{i-1}\right)\left(d_{i-1}-d_{i+1}\right)\right)\right] \\ \gamma_i^{\|} &= d_{i-2}d_{i-1}/\left[d_{i+1}\left(d_{i-1}+d_{i+1}\right)\left(d_{i-2}-d_{i+1}\right)\right] \end{cases}$	(I.3)
Second Derivative $(C_{xx})_i = \alpha_i^{\|\|} C_{i-2} + \beta_i^{\|\|} C_{i-1} - \left(\alpha_i^{\|\|} + \beta_i^{\|\|} + \gamma_i^{\|\|} \right) C_i + \gamma_i^{\|\|} C_{i+1} + \epsilon_i^{\|\|}$	(I.4)
Three-point central-difference scheme $\alpha_i^{\|\|} = 0 \quad \beta_i^{\|\|} = 1/\left(d_{i-1}\Delta x_i\right) \quad \gamma_i^{\|\|} = 1/\left(d_{i+1}\Delta x_i\right)$	(I.5)
Higher order scheme $\begin{cases} \alpha_i^{\|\|} = 2\left(d_{i+1}-d_{i-1}\right)/\left[d_{i-2}\left(d_{i-2}+d_{i+1}\right)\left(d_{i-2}-d_{i-1}\right)\right] \\ \beta_i^{\|\|}2 = 2\left(d_{i-2}-d_{i+1}\right)/\left[d_{i-1}\left(d_{i-2}-d_{i-1}\right)\left(d_{i-1}+d_{i+1}\right)\right] \\ \gamma_i^{\|\|} = 2\left(d_{i-1}+d_{i-1}\right)/\left[d_{i+1}\left(d_{i-1}+d_{i+1}\right)\left(d_{i-2}+d_{i+1}\right)\right] \end{cases}$	(I.6)
$d_{i-2} \equiv \Delta x_{i-1} + \left(\Delta x_{i-2} + \Delta x_i\right)/2 \qquad d_{i-1} \equiv \left(\Delta x_{i-1} + \Delta_i\right)/2 \qquad d_{i+1} \equiv \left(\Delta x_i + \Delta x_{i+1}\right)/2$	

TABLE I. Finite difference methods for 1st and 2nd derivatives used within the **BurnupFunction**. C_i terms represent a Taylor series expansion, and Δx_i is the distance between at points (i) on the secondary grid.

The initial implementation followed were one-point upstream and a three-point central-difference for first and second derivatives, respectively, as seen in Table I. These methods, while relatively easy to implement, introduce accuracy errors due to truncation and utilizing an inferior procedure of solving the finite difference problems using linear algebra methods. As shown in Liu's paper and Table II, the results indicate that, as grid nonuniformity becomes important, the higher order formulation maintains greater accuracy while the lower order formulations become less accurate and produce larger errors with additional numerical dispersion. The numerical solutions computed by the schemes using these conventional formulas are no longer suitable. The higher order scheme gives a better numerical approximation to the analytical solutions compared with those of the other schemes and achieves a wide range of flexibility in designing nonuniform grids.

Finite-Difference Scheme Orders of Accuracy			
Scheme	**Truncation Error Coefficient**	**Order of Accuracy**	
First Derivative			
One-point upstream			
Uniform spacing	$\tau_1^{\mid} \neq 0$	$O\left(\Delta x\right)$	(II.1)
Nonuniform spacing	$\tau_1^{\mid} \neq 0$	$O\left(\Delta x\right)$	(II.2)
Higher order scheme			
Uniform spacing	$\tau_1^{\mid} = 0 \quad \tau_2^{\mid} = 0 \quad \tau_3^{\mid} \neq 0$	$O\left(\Delta x^3\right)$	(II.3)
Nonuniform spacing	$\tau_1^{\mid} = 0 \quad \tau_2^{\mid} = 0 \quad \tau_3^{\mid} \neq 0$	$O\left(\Delta x^3\right)$	(II.4)
Second Derivative			
Three-point central difference			
Uniform spacing	$\tau_1^{\mid\mid} = 0 \quad \tau_2^{\mid\mid} \neq 0$	$O\left(\Delta x^2\right)$	(II.5)
Nonuniform spacing	$\tau_1^{\mid\mid} \neq 0$	$O\left(\Delta x\right)$	(II.6)
Higher order scheme			
Uniform spacing	$\tau_1^{\mid\mid} = 0 \quad \tau_2^{\mid\mid} \neq 0$	$O\left(\Delta x^2\right)$	(II.7)
Nonuniform spacing	$\tau_1^{\mid\mid} = 0 \quad \tau_2^{\mid\mid} \neq 0$	$O\left(\Delta x^2\right)$	(II.8)

TABLE II. Order of accuracy for finite-difference schemes used with BISON **BurnupFunction**. Truncation errors for 1st and 2nd derivatives are defined in Table III.

Coefficients of the Truncation Error

First Derivative

$$\epsilon_i^1 = \tau_1^| \Delta x \left(C_{xx}\right)_i + \tau_2^| \Delta x^2 \left(C_{xxx}\right)_i + \tau_3^| \Delta x^3 \left(C_{xxxx}\right)_i + HOT$$

$$\tau_1^| = -\left(\alpha_i d_{i-2}^2 + \beta_i d_{i-1}^2 + \gamma_i d_{i+1}^2\right) / \left(2\Delta x\right)$$

$$\tau_2^| = -\left(\alpha_i d_{i-2}^3 - \beta_i d_{i-1}^3 + \gamma_i d_{i+1}^3\right) / \left(6\Delta x^2\right)$$

$$\tau_3^| = -\left(\alpha_i d_{i-2}^4 + \beta_i d_{i-1}^4 + \gamma_i d_{i+1}^4\right) / \left(24\Delta x^3\right)$$

Second Derivative

$$\epsilon_i^1 = \tau_1^{||} \Delta x \left(C_{xxx}\right)_i + \tau_2^{||} \Delta x^2 \left(C_{xxxx}\right)_i + HOT$$

$$\tau_1^| = -\left(-\alpha_i d_{i-2}^3 - \beta_i d_{i-1}^3 + \gamma_i d_{i+1}^3\right) / \left(6\Delta x\right)$$

$$\tau_2^| = -\left(\alpha_i d_{i-2}^4 - \beta_i d_{i-1}^4 + \gamma_i d_{i+1}^4\right) / \left(24\Delta x^2\right)$$

TABLE III. Coefficients of the truncation error for 1st and 2nd derivatives using finite-difference methods. The coefficients for separate schemes have been determined and displayed in Table II.

Due to the nature of the problems being investigated, differential equations are common. The finite-difference scheme chosen directly determines the method of linear algebra used to solve these differential equations. Each finite-difference scheme has its own inaccuracies, which are multiplied within the linear algebra method used to solve the equations. The intention of this effort is to reduce errors while providing a simple yet efficient method of computation. The description of these methods and the applications follow.

B. Fission Effective Probability

The subroutine for the fission effective probability within the **BurnupFunction** is used in creating the RPF. The RPF within the **BurnupFunction** represents the power generated from the fission processes on the isotopes composing the fuel. In an LWR, this is a complicated function of radial position, initial enrichment, and operating conditions in addition to the fission processes occurring. The effective probability is calculated as a function of the fission cross-sections and isotope concentrations and helps in crafting the RPF.

Initially, the determination of the effective probability of fission occurring for each isotope was determined using the three-point central-difference scheme. This algorithm was used as a curvature correction on the second derivative for decreasing fission probability, and as a result, the RPF at low radial positions. This procedure was upgraded to utilize the higher order scheme to ensure greater fidelity in the radially dependent positions. As seen in Table II, the order of accuracy between the three-point central difference and higher order scheme are both 2nd order with respect to uniform grid spacing.

The important changes come for nonuniform spacing where the higher order scheme outperforms the three-point central difference.

Since the fission effective probability limits terms in a regressive fashion, the furthest radial points must numerically use the three-point central difference (i.e., there isn't a point for the C_{i+2} coefficient). While the 2nd derivative test is only a check for the inflection by checking the sign of the result, the secondary grid spacing and fission probabilities from different isotopes can result in an answer of zero for the three-point central difference scheme. An answer of zero for the 2nd derivative test requires a higher order test to give conclusive results. To avoid this conclusion, using the higher order scheme helps prevent this result by taking more points to ensure a definite conclusion.

C. Neutron Diffusion

Following historic precedent, the neutron diffusion equation is solved in one-dimensional cylindrical coordinates by finite difference. This term, combined with the fission probability, creates the RPF. Within this subroutine, numerous parts needed to be upgraded to provide consistent physical results. The primary driving change was the method in which the numerical linear algebraic method is used to solve the diffusion equation.

The time-independent neutron diffusion equation in one-dimensional cylindrical coordinates is solved by:

$$\nabla^2 \phi - \frac{1}{L^2}\phi = -\frac{s}{D} \tag{1}$$

where

ϕ is the neutron flux
D is the diffusion coefficient
s is the neutron source rate
Σ_a is the macroscopic absorption cross section
$L^2 \equiv \frac{D}{\Sigma_a}$

Solving for a point source eliminates s, thus in cylindrical coordinates:

$$\frac{1}{r}\frac{\partial}{\partial r}\left(r\frac{\partial \phi}{\partial r}\right) + \frac{1}{r^2}\frac{\partial^2 \phi}{\partial \theta^2} + \frac{\partial^2 \phi}{\partial z^2} - \frac{1}{L^2}\phi = 0 \tag{2}$$

Using separation of variables, with:

$$\phi\left(r, \varphi, \theta\right) = R\left(r\right)\Theta\left(\theta\right)Z\left(z\right)$$

Assuming the solution is at a constant height z and is cylindrically invariant yields:

$$\phi\left(r\right) = R\left(r\right)$$

$$\frac{d^2 \phi}{dr^2} + \frac{1}{r}\frac{d\phi}{dr} - k^2\phi = 0 \tag{3}$$

where
$$k^2 = \frac{1}{L^2}$$

Using Table I, with Equations (I.1) and (I.4) for the 1st and 2nd derivatives, respectively, Equation (II-C) can be solved as a finite-difference problem. Initially, this was solved using Equations (I.2) and (I.5), which results in:

$$\beta_i^{||} C_{i-1} - \left(\beta_i^{||} + \gamma_i^{||}\right) C_i + \gamma_i^{||} C_{i+1} + \frac{1}{r} \left(\beta_i^{|} C_{i-1} - \beta_i^{|} Ci\right) - k^2 C_i$$

Rearranging this:

$$\left(\frac{\beta_i^{|}}{r} + \beta_i^{||}\right) C_{i-1} + \left(-\beta_i^{||} - \gamma_i^{||} - \frac{\beta_i^{|}}{r} - k^2\right) C_i + \gamma_i^{||} C_{i+1}$$

This is a linear algebra problem, $a_i x_{i-1} + b_i x_i + c_i x_{i+1} = d_i$, which can be solved by the tridiagonal matrix algorithm, sometimes called the Thomas algorithm. This is represented in linear algebra as:

$$\begin{bmatrix} b_0 & c_0 & & & 0 \\ a_1 & b_1 & c_1 & & \\ & a_2 & b_2 & \ddots & \\ & & \ddots & \ddots & c_{n-2} \\ 0 & & & a_{n-1} & b_{n-1} \end{bmatrix} \begin{bmatrix} x_0 \\ x_1 \\ x_2 \\ \vdots \\ x_{n-1} \end{bmatrix} = \begin{bmatrix} d_0 \\ d_1 \\ d_2 \\ \vdots \\ d_{n-1} \end{bmatrix}. \tag{4}$$

This algorithm is efficient and only requires $O(n)$ operations for the forward and back substitutions required for the lower–upper (LU) decomposition. The forward substitution eliminates the a_i terms, and then backward substitution produces the solution. Storing the full $N \times N$ matrix is not required in that only the non-zero components can be stored. Pivoting is not required, which leads to possible failures even when the matrix is non-singular. In general, this algorithm is valid when:

$$|b_i| > |a_i| + |c_i| \qquad j = 0, \ldots, N-1$$

While most linear algebra representations resulting from the finite-difference representation of partial differential equations satisfy this condition, it is not guaranteed. If this algorithm produces numerically unstable results, pivoting through standard LU decomposition methods must be followed. Irregularities in the RPF led to the discovery that the criterion was not being met and that a banded matrix approach would be necessary.

As was similarly done for the original implementation, using Equations (I.1 and (I.4) for the 1st and 2nd derivatives, respectively, from Table I, except using Equations (I.3) and (I.6), results in:

$$\left(\frac{\alpha_i^{|}}{r} + \alpha_i^{||}\right) C_{i-2} + \left(\frac{\beta_i^{|}}{r} + \beta_i^{||}\right) C_{i-1}$$

$$+ \left(-\alpha_i^{|} - \beta_i^{||} - \gamma_i^{||} - \frac{\alpha_i^{|}}{r} - \frac{\beta_i^{|}}{r} - \frac{\gamma_i^{|}}{r} - k^2\right) C_i + \left(\gamma_i^{||} + \frac{\gamma_i^{|}}{r}\right) C_{i+1} =$$

This is a linear algebra problem, $a_i x_{i-2} + b_i x_{i-1} + c_i x_i + d_i x_{i+1} = e_i$, which in the new implementation is solved by using a band diagonal method, as outlined in Numerical Recipes in C++ (Press and Vetterling, 2007). This method allows for stability and greater flexibility for future improvements, in addition to reduced truncation errors. In matrix form:

$$
\begin{bmatrix}
c_0 & d_0 & & & & & 0 \\
b_1 & c_1 & d_1 & & & & \\
a_2 & b_2 & c_2 & d_2 & & & \\
& a_3 & b_3 & c_3 & d_3 & & \\
& & \ddots & \ddots & \ddots & d_{n-2} & \\
0 & & & a_{n-1} & b_{n-1} & c_{n-1}
\end{bmatrix}
\begin{bmatrix}
x_0 \\ x_1 \\ x_2 \\ x_3 \\ \vdots \\ x_{n-1}
\end{bmatrix}
=
\begin{bmatrix}
e_0 \\ e_1 \\ e_2 \\ e_3 \\ \vdots \\ e_{n-1}
\end{bmatrix}.
\tag{5}
$$

This requires an addition vector to be stored of non-zero diagonal components and adds several additional steps. The decomposition of the compact matrix follows Crout's method, producing a lower triangular matrix (L) and an upper triangular matrix (U). Then after this pivoting, following forward and backward substitutions, the solution to the problem can be found. The $O(n^3)$ operations is greater than the Thomas method, but the method is robust unlike when the tridiagonal matrix is singular.

The limiting of the coefficients used in Matrices (4) and (5) uniquely determines that only the certain terms are valid, independent of the algorithm used, for certain points on the secondary grid. As can be seen in the matrix representation in Equations (4) and (5), for the 0th terms, $\gamma_0^{\|}$ for the C_i, and C_{i+1} are the only valid components. To account for this, at $r = 0$, Equation (II-C) be expanded in the form of a Maclaurin series:

$$
\frac{1}{r}\frac{d\phi}{dr} = \frac{1}{r}\frac{d\phi}{dr} + \frac{1}{r^2}\left(r\frac{d^2\phi}{dr^2} - \frac{d\phi}{dr} \right) r + \dots
$$

$$
\frac{1}{r}\frac{d\phi}{dr} = \frac{1}{r}\frac{d\phi}{dr} + \frac{d^2\phi}{dr^2} - \frac{1}{r}\frac{d\phi}{dr} + \dots
$$

$$
\frac{1}{r}\frac{d\phi}{dr} = \frac{d^2\phi}{dr^2}
\tag{6}
$$

Inserting Equation (6) into Equation (II-C) yields:

$$
2\frac{d^2\phi}{dr^2} - k^2\phi = 0 \qquad \text{at } r = 0
\tag{7}
$$

Using finite difference, the second derivative term in Equation (7) can be solved for as:

$$
\frac{d^2\phi}{dr^2} = \frac{\frac{\phi(r+d)-\phi(r)}{d} - \frac{\phi(r)-\phi(r-d)}{d}}{d}
$$

$$
\frac{d^2\phi}{dr^2} = \frac{\phi(r+d) - 2\phi(r) + \phi(r-d)}{d^2}
$$

where the flux ϕ at:

$$
r = 0 \implies \begin{cases} \phi(d) = \phi(-d) = 1 \\ \phi(0) = 0 \end{cases}
\tag{8}
$$

This allows the second derivative in Equation (7) to be expressed as:

$$2\frac{d^2\phi}{dr^2} = \frac{4}{d}$$

Similarly, at the last point in the secondary grid of order i^{n-1}, the flux $\phi = 1$, which implies derivatives are not necessary. As such, only the C_i term is required with a value of unity. Additionally, this demands the solution to be defined as unity. This constraint is also independent of the finite-difference schema used.

D. Displaced Mesh Concentrations

A major effort in accurately displaying the isotope radial dissemination was undertaken as part of the **BurnupFunction** refactoring. As previously described, the isotope evolution was tracked on a stationary secondary grid, based on the initial mesh conditions. As the physics of the simulation evolves, the mesh changes dynamically to represent the fuel swelling and similar process. The secondary grid does not change but does communicate with the evolving mesh points. When visualizing radial concentrations, the distribution would not account for the fuel expansion and, as a result, show a grouping smaller than the actual end state. To simplify the reporting of isotope dispersal, the displacement of the initial points in the mesh, corresponding to the secondary grid points, were used to create an accurate displaced mapping.

A new class was created named **RadialProfileSampler** to accurately report isotope distributions, as computed by **BurnupFunction**, as the mesh evolves. For a given height, this **VectorPostprocessor** expects a list of quantities to report. These quantities can include N^{235}, N^{236}, N^{238}, N^{239}, N^{239}, N^{240}, N^{241}, N^{242}, fission rate, RPF, and burnup as well as the total number of atoms of heavy metals (*U and Pu at this time*).

As a part of benchmarking, this new class was used with the simulation of the BISON assessment case for High Burnup Effects Programme (HBEP) BK365.This case was chosen because it provides high burnup data on fission gas release and fission product distributions. Rod BK365 was irradiated to 69.4 MWd/KgU in the BR-3 pressurized-water reactor (IAEA, 2002-2007). This specific case was chosen for its relatively short running time, as well as the existence of experimental data on radial isotope distribution from the Transuranium Institute.
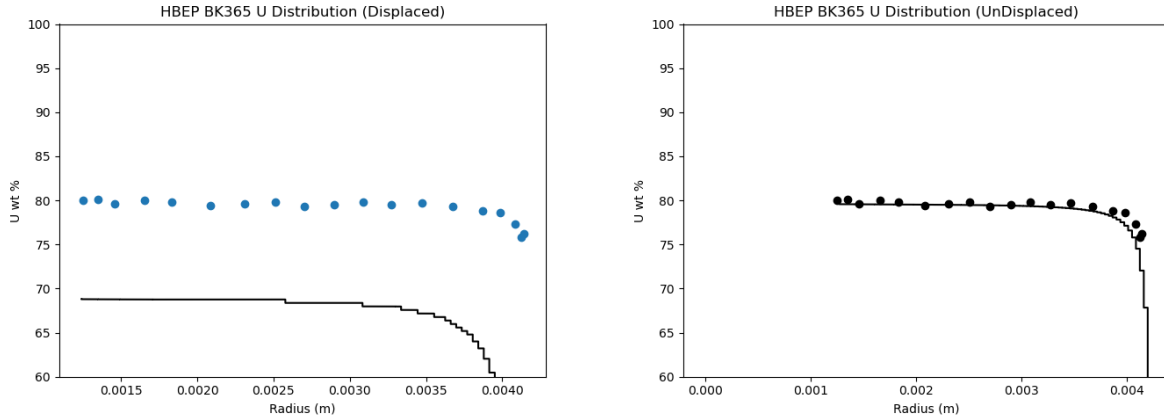
Fig. 1. Uranium radial distribution on the undisplaced (left) and displaced (right) mesh for HBEP BK365. Experimental data is shown as points and the simulation as a line.
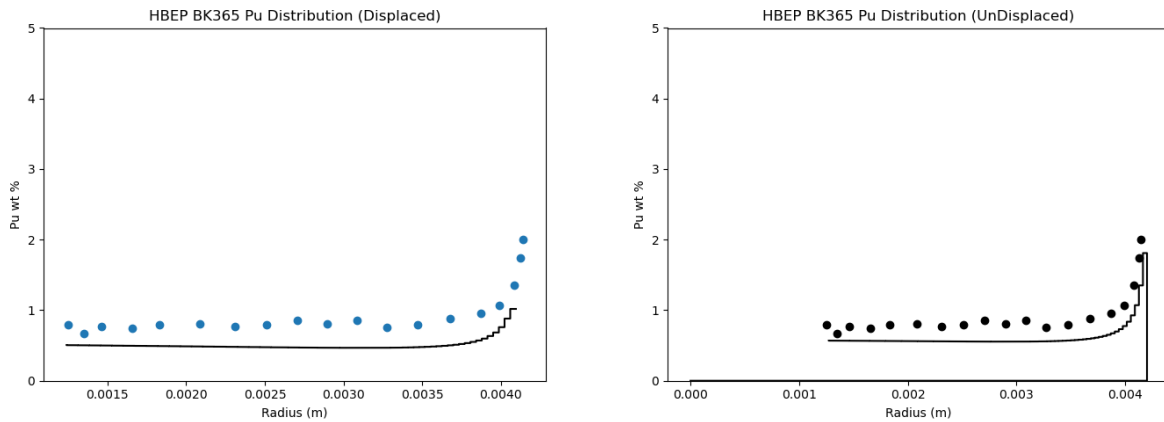
Fig. 2. Plutonium radial distribution on the undisplaced (left) and displaced (right) mesh for HBEP BK365. Experimental data is shown as points and the simulation as a line.

E. Gadolinia effects on the burnup and RPF calculations

For this purpose, BISON uses the DIONISIO model from Soba et al. (2013, 2014); Soba and Denis (2017). This model computes the evolution of the concentrations of various heavy metal isotopes (specifically, ^{235}U, ^{236}U, ^{238}U, ^{239}Pu, ^{240}Pu, ^{241}Pu, ^{242}Pu, ^{155}Gd, and ^{157}Gd) locally across the radius of the fuel pellet and the coupled evolution of the radial power and burnup distributions. The model uses one-group cross sections that are a function of radial position, ^{235}U enrichment, and radially averaged burnup and are fitted to the results of extensive neutronics calculations performed with the CONDOR and HUEMUL codes. Neutronics calculations covered LWR UO$_2$ fuel rods with initial ^{235}U enrichments

from 0.7% to 12% and average burnups ranging from fresh fuel to 120 MWd/kgU (Soba et al., 2013, 2014; Soba and Denis, 2017).

The rate equations describing the evolution of the concentrations of each heavy metal isotope are:

$$\frac{\mathrm{d}\,N_{235}}{\mathrm{d}\,t} = -\sigma_a^{235}\overline{N}_{235}\phi \tag{9a}$$

$$\frac{\mathrm{d}\,N_{236}}{\mathrm{d}\,t} = -\sigma_a^{236}\overline{N}_{236}\phi + \sigma_c^{235}\overline{N}_{235}\phi \tag{9b}$$

$$\frac{\mathrm{d}\,N_{238}}{\mathrm{d}\,t} = -\sigma_a^{238}\overline{N}_{238}\phi \tag{9c}$$

$$\frac{\mathrm{d}\,N_{239}}{\mathrm{d}\,t} = -\sigma_a^{239}\overline{N}_{239}\phi + \sigma_c^{238}\overline{N}_{238}\phi \tag{9d}$$

$$\frac{\mathrm{d}\,N_{240}}{\mathrm{d}\,t} = -\sigma_a^{240}\overline{N}_{240}\phi + \sigma_c^{239}\overline{N}_{239}\phi \tag{9e}$$

$$\frac{\mathrm{d}\,N_{241}}{\mathrm{d}\,t} = -\sigma_a^{241}\overline{N}_{241}\phi + \sigma_c^{240}\overline{N}_{240}\phi \tag{9f}$$

$$\frac{\mathrm{d}\,N_{242}}{\mathrm{d}\,t} = -\sigma_a^{242}\overline{N}_{242}\phi + \sigma_c^{241}\overline{N}_{241}\phi \tag{9g}$$

$$\frac{\mathrm{d}\,N_{155}}{\mathrm{d}\,t} = -\sigma_a^{155}\overline{N}_{155}\phi \tag{9h}$$

$$\frac{\mathrm{d}\,N_{157}}{\mathrm{d}\,t} = -\sigma_a^{157}\overline{N}_{157}\phi \tag{9i}$$

where N is the local concentration (number of atoms per unit volume), σ_a is the absorption cross section, σ_c is the capture cross section, and ϕ is the neutron flux. Note that decay terms are neglected in the BISON implementation. Equations 9(h) and 9(i) are recently integrated into the code to compute Gd effects on the burnup and radial power profiles. Considering the scope of this paper, we only present new changes in the code.

As previously described, the cross sections have been fitted from a single-energy group study using CONDOR. The fit follows a function of:

$$f_1(r, b, q) = a_0 + a_1 r + a_2 b + a_3 r^2 + a_4 r b + a_5 b^2 + a_6 r^3 + a_7 r^2 b + a_8 r b^2 + a_9 b^3 \tag{10}$$

where r is the position in meters on the secondary grid, b is the burnup (MWd/kgU), q is the ^{235}U enrichment (%), and a_0 through a_9 are the empirical coefficients given for the absorption cross sections, as shown in Tables IV and V.

$$a_0 = 1.9339 \times 10^2 - 12.885q - 7.831g$$

$$a_1 = 1.4676 \times 10^2 - 30.342q - 33.965g + 2.7774q^2 + 2.6193g^2$$

$$a_2 = -2.5837 \times 10^3 + 3.4162 \times 10^2 q + 2.5883 \times 10^2 g$$

$$a_3 = \frac{qg}{-0.71656 + 4.4941 \times 10^{-2} \exp{(q)} + 6.7029 \times 10^{-3} \exp{(g)}}$$

$$a_4 = -1.1637 \times 10^4 + 5.8691 \times 10^3 q + 2.6127 \times 10^3 g - 1.1681 \times 10^3 q^2 - 3.1771 \times 10^2 g^2$$
$$+ 75.772q^3 + 7.6019g^3 - 9.1283 \times 10^2 qg + 33.483q^2g + 45.734g^2q$$

$$a_5 = -0.92356 + 6.6888 \times 10^{-2}q + 0.10511g$$

$$a_6 = -8.3028 \times 10^2 + 2.9518 \times 10^3 q + 1.8994 \times 10^3 g - 1.9336 \times 10^2 q^2 - 72.757g^2$$
$$+ 23.589qg$$

$$a_7 = 8.9867 \times 10^2 - 65.205q - 4.5833 \times 10^2 g$$

$$a_8 = -41.393 + 0.90863q + 4.9750g + 0.12383q^2 - 0.24634g^2$$

$$a_9 = -8.0211 \times 10^2 + 60.288q + 62.367g$$

TABLE IV. Gd^{155} absorption cross-section coefficients calculated for a single energy group. Here q is the ^{235}U enrichment (%) and g is the initial gadolinium content (%) (Soba et al., 2014; Soba and Denis, 2017).

$$a_0 = 7.3318 \times 10^3 - 6.7731 \times 10^3 q + 1.6764 \times 10^3 g + 1.5868 \times 10^3 q^2 - 1.7375 \times 10^2 g^2$$
$$- 1.0986 \times 10^2 q^3 + 5.7503 g^3 - 2.4407 \times 10^2 qg + 8.8016 q^2 g + 1.1284 \times 10^1 g^2 q$$

$$a_1 = 6.4762 \times 10^2 - 1.3052 \times 10^2 q - 1.5197 \times 10^2 g + 1.1948 \times 10^1 q^2 + 1.169 \times 10^1 g^2$$

$$a_2 = -1.1121 \times 10^4 + 1.4610 \times 10^2 q + 1.1090 \times 10^3 g$$

$$a_3 = \frac{qg}{-1.7177 \times 10^{-1} + 1.0722 \times 10^{-2} \exp(q) + 1.5135 \exp(g)}$$

$$a_4 = 1.7696 \times 10^4 - 5.5024 \times 10^3 q - 5.0299 \times 10^3 g$$

$$a_5 = -1.3180 \times 10^1 + 1.3711 q + 3.3317 g - 1.0730 \times 10^{-1} q^2 - 2.3917 \times 10^{-1} g^2$$

$$a_6 = 1.9835 \times 10^4 + 4.9922 \times 10^3 q + 4.9244 \times 10^3 g$$

$$a_7 = 3.8504 \times 10^3 - 2.7806 \times 10^2 q - 1.9614 \times 10^2 g$$

$$a_8 = -1.6426 \times 10^2 - 5.1839 \times 10^{-1} q + 2.1626 \times 10^1 g + 8.9344 \times 10^{-1} q^2 - 1.097 g^2$$

$$a_9 = -4.2786 \times 10^3 + 5.5727 \times 10^2 q + 3.3387 \times 10^2 g - 2.9959 \times 10^1 q^2 - 5.5259 g^2$$

TABLE V. Gd^{157} absorption cross-section coefficients calculated for a single energy group. Here q is the ^{235}U enrichment (%) and g is the initial gadolinium content (%) (Soba et al., 2014; Soba and Denis, 2017).

Passing a function for the RPF exists within the **BurnupFunction** class, and an initial implementation accounting for gadolinium doping within fuel was implemented in 2020 for the IFA 681 rod3 assessment case. The Halden integral test IFA-681 was loaded in the Halden Boiling Water Reactor in January 2005 and operated until February 2012 completing 15 cycles of irradiation. The rig contained two UO_2 fuel rods and four UO_2-Gd_2O_3 rods with varied gadolinia content from 0.0 to 8.0 wt%. The experiment was conducted under standard Halden Boiling Water Reactor conditions, with the rig operating at a coolant pressure of approximately 3.5 MPa and a coolant temperature of approximately 235°C, and achieved burnup varied between 31 and 45 MWd/kgUO$_2$. The aim in the experiment was to evaluate the impact of Gd concentration on the fuel thermal behavior, dimensional changes, and fission gas release. The supplementary histories, from Halden data, such as linear heat rate, fast neutron flux, coolant pressure, and coolant inlet temperatures are provided to BISON. The Fuel Rod Analysis Toolbox is utilized for the condensation of the data prior to setting the BISON inputs. Radial power factors are computed at the IFE-Halden Reactor Project via the HELIOS code ((Stammler, 2000) (Kim, 2003)) to inform the BISON analysis, as seen in Fig 3.
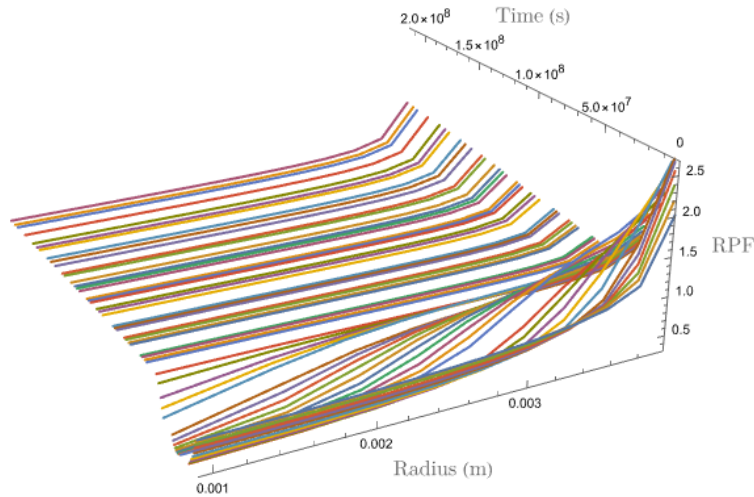
Fig. 3. Prescribed RPF used on the IFA 681 Rod 3 assessment case in BISON. The prescribed RPF has 59 "lines" applied at specific time points.

Using the IFA 681 Rod 3 case, which has a 8% Gd weight by distribution, comparisons of the prescribed and coefficient methods were investigated. As shown in Fig 4, the RPF varies as would be expected due to the effects of gadolinium instead of the use of prescribed functions. These effects are more apparent as shown in Fig 5 where the isotropic distribution via the prescribed function shows a constant radial distribution of UO_2 instead of an actual RPF as shown by the use of Gd coefficients. The **BurnupFunction** does not currently have the ability to change the isotropic concentrations when an RPF is specified via a function.
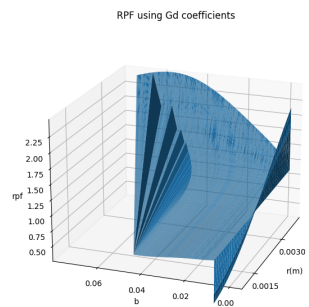
(a) Gd coefficient method
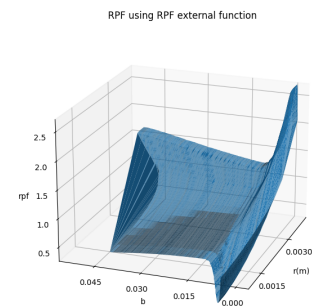
(b) Prescribed RPF

Fig. 4. Comparison of Gd coefficients (left) versus a prescribed RPF input (right). The plots are not identical, nor are they expected to be due to the effects of gadolinium
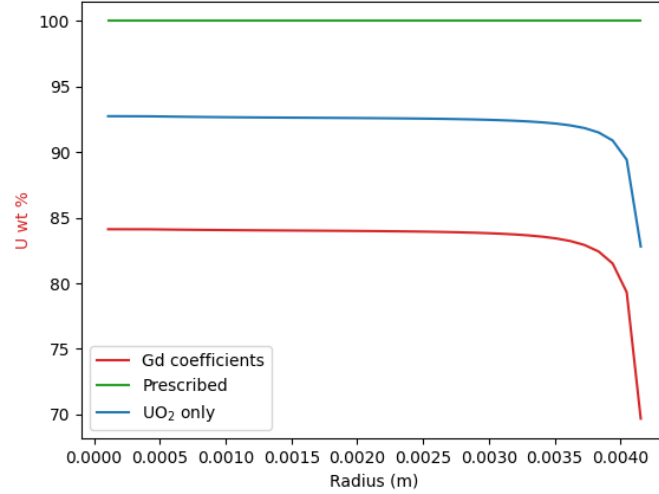
Fig. 5. End-point radial isotopic distribution for prescribed and Gd coefficients. The prescribed method does not account for Gd isotopes, which increases the relative amount of uranium. When accounting for gadolinium, the relative percentage by weight is decreased, as shown in the difference between Gd and UO_2 plots.

F. Limitations on Method

Currently, within the **BurnupFunction**, only UO_2 and U_3Si_2 fuels for LWR are modeled. The method following the Sobe et al. has several restraints that limit the usage in modeling UO_2 and similar fuel burnup. Sobe et al. has expanded the scope of DIONISO, and it is planned the BISON team will develop newer models for newer fuels and reactors in the future. The limitations experienced currently, and the possible solutions, within the **BurnupFunction** are discussed here.

The main limitation of the model is the restriction on the initial fuel enrichment of ^{235}U of $0.7\% - 12\%$ with a max burnup of 120 MWd/kgHM. As a result, this restricts studies with extremely high ^{235}U concentrations or high burnup. The methods utilized by Sobe et al. in determining the cross sections for each isotopes involved a time evolution simulation of fuel pellets within the CONDOR nuclear fuel calculation package. The radial evolution of ^{235}U, ^{236}U, ^{238}U, ^{239}Pu, ^{240}Pu, ^{241}Pu, and ^{242}Pu were used to fit functions representing the absorption, capture, and fission cross sections. This simplified modeling approach shows good agreement with experimental results as shown by Soba et al. ((Soba et al., 2013)). An unfortunate oversight was discovered that several assessment cases within the BISON repository were using this model for ^{235}U concentrations of 13%, which gave nonphysical results with respect to burnup. These miscalculations have been accounted for, and a newer, higher burnup model is being investigated.

The method used to calculate the neutron flux, and in turn the cross sections, is limited to one energy group (thermal neutrons with $E < 0.65eV$). Moreover, the method used to calculate the flux is by assuming neutron diffusion in cylindrical coordinates for a given height z. This limits the fuel geometry

to only traditionally cylindrical shapes. While it is considered to be one-dimensional spherical coordinates, the Laplacian is slightly different for this geometry and results in neglecting higher energy flux and the nonisotropic distribution. Having multiple energy groups is feasible and recommended to better model fast flux effects, such as cladding creep.

An additional shortcoming within the **BurnupFunction** is the limitation of the isotopes being tracked. While the half-lives of the uranium and plutonium isotopes currently tracked within the model far exceed the time scale of the fuel cycle, in general, transmutation and decay are not considered. For the fission products, which are often measured experimentally, having a more accurate representation of fuel evolution is necessary. As a part of refactoring, and discussed in more depth in the previous section, ^{155}Gd and ^{157}Gd as burnable poisons have been added to the isotopes being tracked. Adding the ability to better model fuel depletion and isotropic evolution is attainable following the same method by developing bicubic interpolation functions for cross sections of interest.

III. Fuel Creep

A. Improvements to the UO_2 fuel creep model

1) MATPRO fuel creep model overview

Fuel creep deformation in BISON is calculated using a previously-developed semi-empirical model which incorporates both thermal and irradiation creep deformation mechanisms. This model is central to predicting the deformation behavior of several nuclear fuel-cladding concepts, especially those that undergo pellet-cladding mechanical interaction. As such, LWR assessment cases in BISON which utilize UO_2 fuel rely on the MATPRO creep model for accurate comparisons to experimental measurements. This model is semi-empirical and thus contains several parameters that have historically been determined through least-squares regression and could benefit from being calibrated with additional data.

The thermal and irradiation creep strain rates for UO_2 are calculated by the MATPRO model, as described by Allison et al. (Allison et al. (1993)), and are used in BISON fuel performance calculations. This model is important for integral fuel performance to identify the impact of fuel compliance, primarily from the contribution from various creep mechanisms, on cladding stress state and subsequent deformation. This correlation, shown in Equation (11), is defined by three separate creep rate contributions based on the expected deformation mechanism; irradiation-enhanced thermal creep (grain boundary sliding/diffusional creep), thermal creep (dislocation climb and glide), and fission-induced creep (athermal creep from fission).

$$\dot{\epsilon}_{total} = \frac{A_1 + A_2 \dot{F}}{(A_3 + D)G^2} \sigma \exp\left(\frac{-Q_1}{RT}\right) + \frac{A_4}{(A_6 + D)} \sigma^{4.5} \exp\left(\frac{-Q_2}{RT}\right) + A_8 \dot{F} \sigma \exp\left(\frac{-Q_3}{RT}\right) \quad (11)$$

where $\dot{\epsilon}_{total}$ is the creep strain rate of the fuel (1/s), A_x are various fitting constants in the model (defined in Table VI), $\dot{F}$ is the fission rate (#/m^3-s), D is the fuel density expressed as a percent of theoretical density (% TD), G is the grain size (µm), Q_x are the thermal activation energies for each creep contribution (J/mol), σ is the effective stress in the fuel (Pa), T is the temperature of the fuel (K), and R is the universal gas constant (8.3145 J/mol-K).

The thermal activation energies for the first two creep contributions, Q_x, are a function of the fuel stoichiometry. Equations (12)–(13) show the activation energies using a function of the fuel oxide-to-metal ratio. The fission-induced creep thermal activation energy, Q_3, has not been shown to have a stoichiometry dependence. Equation (15) modifies the activation energies with an increasing fuel oxide-to-metal (O/M) ratio. As the O/M ratio increases, the activation energies are reduced, eventually to a constant value as the stoichiometry function reaches zero.

$$Q_1 = 83,143 f(x) + 469,191 \qquad (J/mol) \qquad (12)$$

$$Q_2 = 74,829 f(x) + 301,762 \qquad (J/mol) \qquad (13)$$

$$Q_3 = 21759 \qquad (J/mol) \qquad (14)$$

$$f(x) = \frac{1}{\exp\left(\frac{-20}{log(x-2)} - 8\right) + 1}$$ (15)

TABLE VI. Model constants for the MATPRO fuel creep model (Allison et al. (1993), Hales et al. (2014)).

Model Parameter	Value	Units
A_1	0.3919	$\mu\text{m}^2\text{-Pa}^{-1}\text{-s}^{-1}$
A_2	$1.31e\text{-}19$	$\mu\text{m}^2\text{-m}^3\text{-Pa}^{-1}$
A_3	-87.7	Dimensionless
A_4	$2.0391e\text{-}25$	$\text{Pa}^{-4.5}\text{-s}^{-1}$
A_6	-90.5	Dimensionless
A_8	$3.72264e\text{-}35$	$\text{m}^3\text{-Pa}^{-1}$

Figure 6 shows a logarithmic comparison of the creep rate calculated via the MATPRO model vs. experimentally measured creep rates from various literature sources. The UO$_2$ fuel creep samples compiled in this work include: compression tests (Poteat and Yust (1966), Bohaboy et al. (1969), Sykes and Sawbridge (1969), Brucklacher et al. (1970), Perrin (1971), Burton et al. (1973), Burton and Reynolds (1973), Slagle (1984), Sakai (2013), Sakai et al. (2011)), tension (Solomon and Gebner (1972)) of helical UO$_2$ springs, and bending tests (Wolfe and Kaufman (1967), Clough (1970)). The testing conditions of these fuel experiments span many different fuel manufacturing parameters as well as different loading, irradiation, and temperature conditions. In this figure, creep tests by the various authors vary by marker color, while the marker shape indicates whether or not the experiments include irradiation triangular markers in this figure indicate thermal creep conditions only, while circular markers indicate the experiment included the effect of fissioning fuel. The irradiated experiments at low-strain rates show generally larger disagreements with the calculated MATPRO creep rates. This disagreement motivated a new effort to identify the source of this inaccuracy and improve the model calculations.

The original data and model formulation were revisited, specifically the data used to construct the fission-induced creep contribution, as new creep data experiments (Sakai et al. (2011), Sakai (2013)) indicate an overprediction in the creep rate at lower temperatures. The fission-induced creep contribution (last term) in this model contains a thermal activation energy for a diffusion creep mechanism; although theoretically, this mechanism is thought to be athermal. In order to test this assumption, the exponential activation energy was removed. Equation 16 shows this change in the original fission-induced creep contribution to the athermal form suggested by Solomon et al. (Solomon et al. (1971)). The prefactor A_7 was then edited ($A_7 = 7.78 \times 10^{-37}$) to better reflect newer creep experiments (Sakai (2013)).

$$A_8\dot{F}\sigma\exp\left(\frac{-Q_3}{RT}\right) \rightarrow A_7\dot{F}\sigma$$ (16)

$$\dot{\epsilon}_{total} = \frac{A_1 + A_2\dot{F}}{(A_3 + D)G^2}\sigma\exp\left(\frac{-Q_1}{RT}\right) + \frac{A_4}{(A_6 + D)}\sigma^{4.5}\exp\left(\frac{-Q_2}{RT}\right) + A_7\dot{F}\sigma$$ (17)

This modified model, shown in Equation 17 is the current model form for UO$_2$ creep deformation used in BISON, and while it offers a better agreement with the material physics, the model was additionally

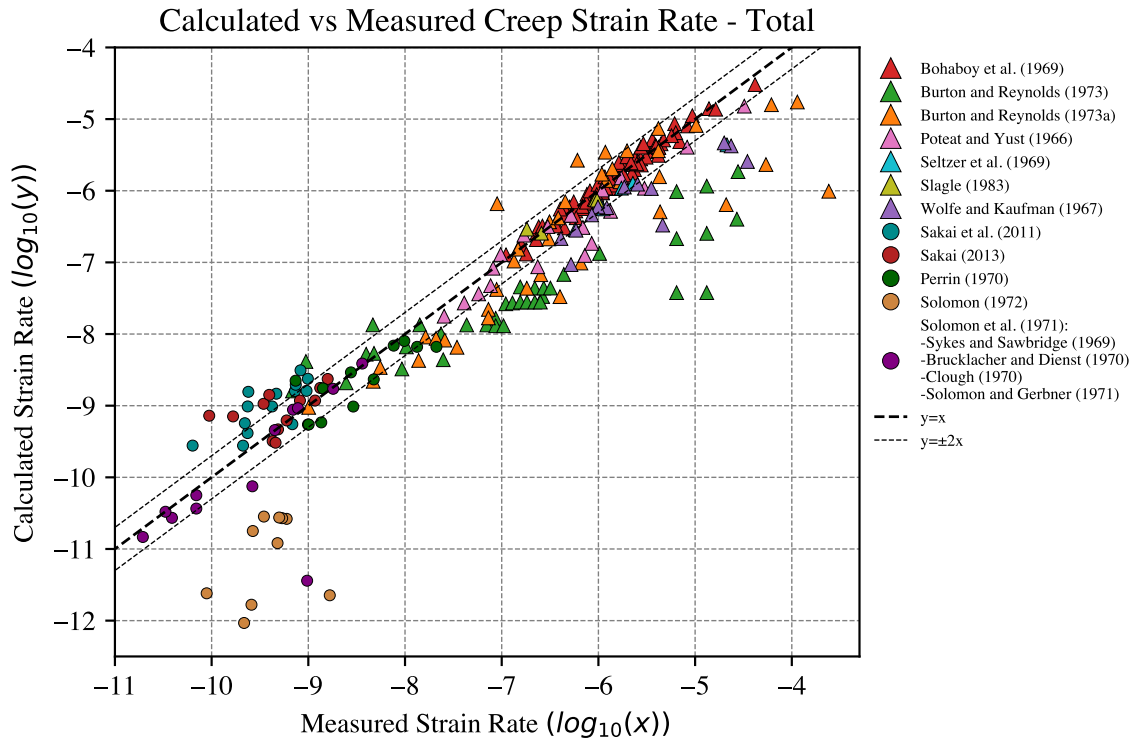Fig. 6. Measured vs. calculated creep strain rates from various fuel creep experiments using the original MATPRO expression. Triangle markers indicate thermal creep only, circle markers indicate irradiation.

improved through parameter calibration using this additional data. In order to perform this calibration, a least-squares fitting algorithm was used on the parameters of this functional form to optimize them.

2) Refitting UO_2 fuel creep model parameters

The parameters for this model were refit to better reflect the accumulated data from the literature. This was performed sequentially based on the phenomena measured and started with the effect of the fuel stoichiometry, thermal creep, and irradiation creep. Because various experiments targeted how different fuel characteristics affected the fuel creep deformation rate, corresponding data was used for the matching fit. Because the creep rate measurements span nearly eight orders of magnitude, the fitting process used the log_{10} of the creep rate. This ensured that very low creep rates would be weighted the same as the higher creep rates, and thus the fitting metrics (RMSE, R^2) used for this effort correspond to logarithmic values.

First, the stoichiometry component of the creep equations were fit. Specifically, the parameters in the oxygen-to-metal weighing factor (Equation 18) and creep activation energy correlations (Equations 19 and 20) were changed. Table VII shows the original parameters used in the original MATPRO fit and the updated parameters from this fit.

$$f(x) = \frac{1}{\exp\left(\frac{F_1}{log(x-2)} - F_2\right) + 1} \tag{18}$$

$$Q_1 = Q_{1a}f(x) + Q_{1b} \qquad (J/mol) \tag{19}$$

$$Q_2 = Q_{2a}f(x) + Q_{2b} \qquad (J/mol) \tag{20}$$

TABLE VII. Original and refitted stoichiometry parameters and activation energies.

Model Parameter	Original Value	Refit Value	Units
Q_{1a}	$83,143$	$118,243$	J/mol
Q_{1b}	$469,191$	$418,012$	J/mol
Q_{2a}	$74,829$	$66,056$	J/mol
Q_{2b}	$301,762$	$309,624$	J/mol
F_1	-20	-13.20	Dimensionless
F_2	8	4.46	Dimensionless

The O/M weighting factor decreases more initially with increasing excess oxygen but remains slightly larger at greater excess oxygen contents (as illustrated in Figure 7). The Q_1 creep activation constant decreased substantially, driven by the decrease in the Q_{1b} parameter refit. The Q_2 parameter remained very similar to the original value. Figure 8 shows a comparison between the original and refit activation energies. Decreasing the Q_1 activation energy implies the irradiation-assisted diffusion or grain boundary sliding creep mechanisms will now be more prominent at lower temperatures.

For each fitting series, plots were generated to show how the calculated-to-measured creep rate agreement changed versus the original data set. These figures, along with the fitting metrics, allowed us to assess how the refitting was affecting the calculated creep rate. Figure 9 shows the comparison for the fuel stoichiometry refit. There is a general increase across nearly all calculated creep rates, and most prominently, several of the high creep rate outliers are moved further into agreement.
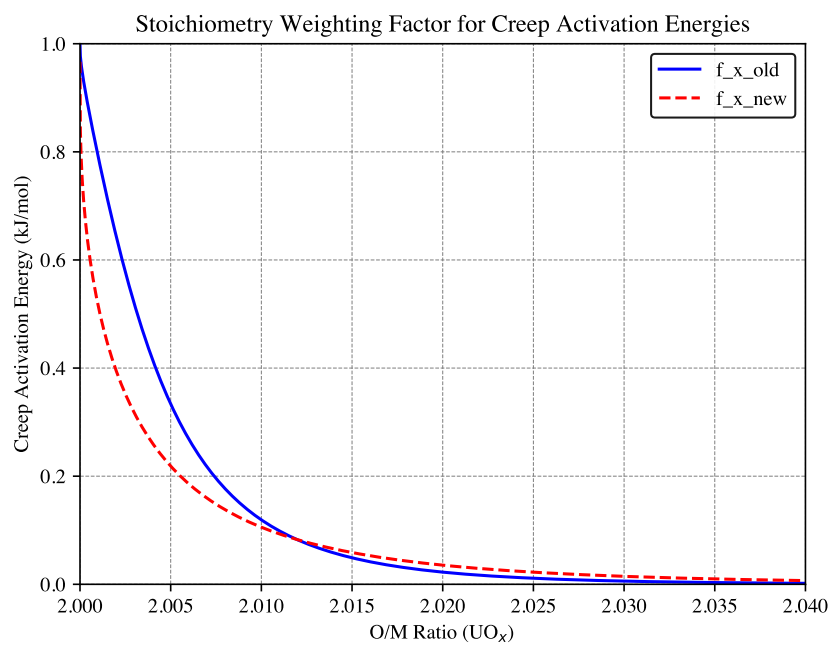
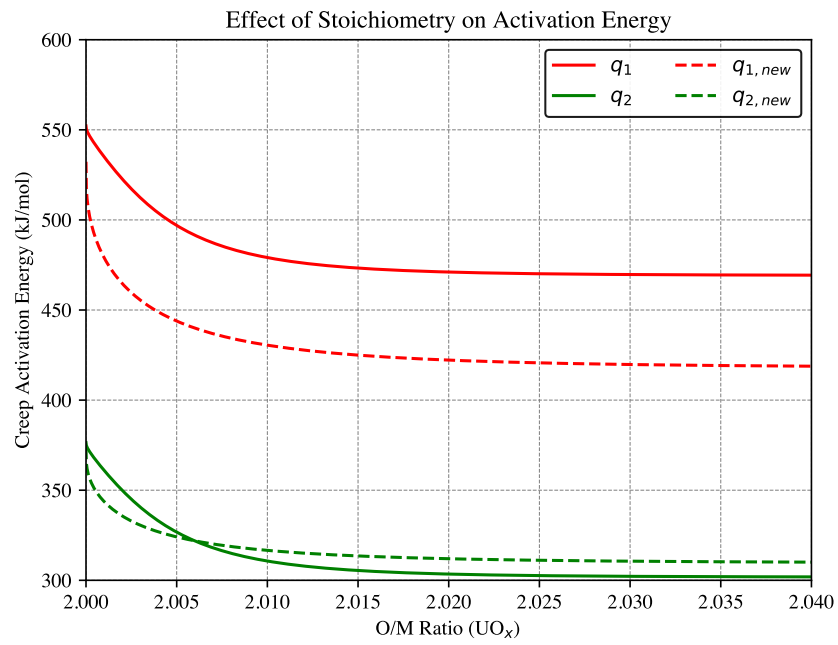Fig. 7. Original (old) and updated (new) stoichiometry functions with increasing fuel excess oxygen.

Fig. 8. Original (old) and updated (new) creep activation energies with increasing fuel excess oxygen.
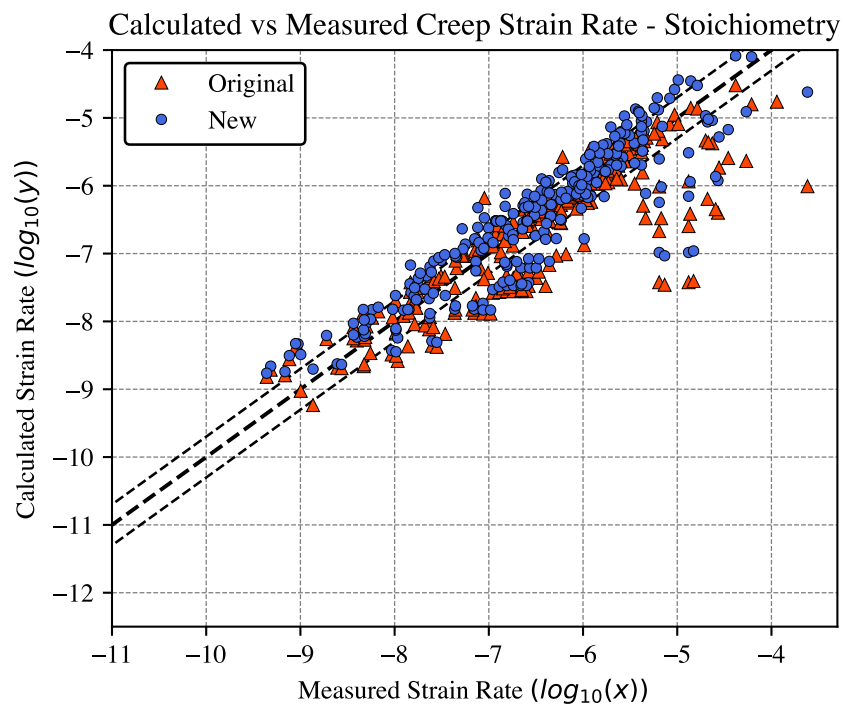
Fig. 9. Measured vs. calculated creep strain rates from using the original MATPRO expression (original) and the updated stoichiometry parameters (new). The thick dashed black line is agreement and thin dashed lines are a factor of two.

The next parameters which were refit targeted the thermal creep behavior. This included the creep prefactors for the first two creep contributions (thermal component of the irradiation-assisted creep and the pure thermal creep) along with the stress exponents of those terms (Equation 17). Most notably, the stress exponent increased for the dislocation creep term while the prefactor decreased, this indicates an increased sensitivity to applied stress. In comparison to the stoichiometry refit, the changes in the calculated creep rate are less apparent in the data spread; although, there is a similar improvement in the agreement according to the fitting metrics, shown in Table X.

TABLE VIII. Original and refitted thermal creep and stress parameters.

Model Parameter	Original Value	Refit Value	Units
A_1	0.3919	1.4376	μm^2-Pa^{-1}-s^{-1}
A_3	-87.7	-66.8	Dimensionless
A_4	$2.0391e$-25	$7.1881e$-34	$Pa^{-4.5}$-s^{-1}
A_6	-90.5	-35.4	Dimensionless
Stress exponent	4.5	5.717	Dimensionless
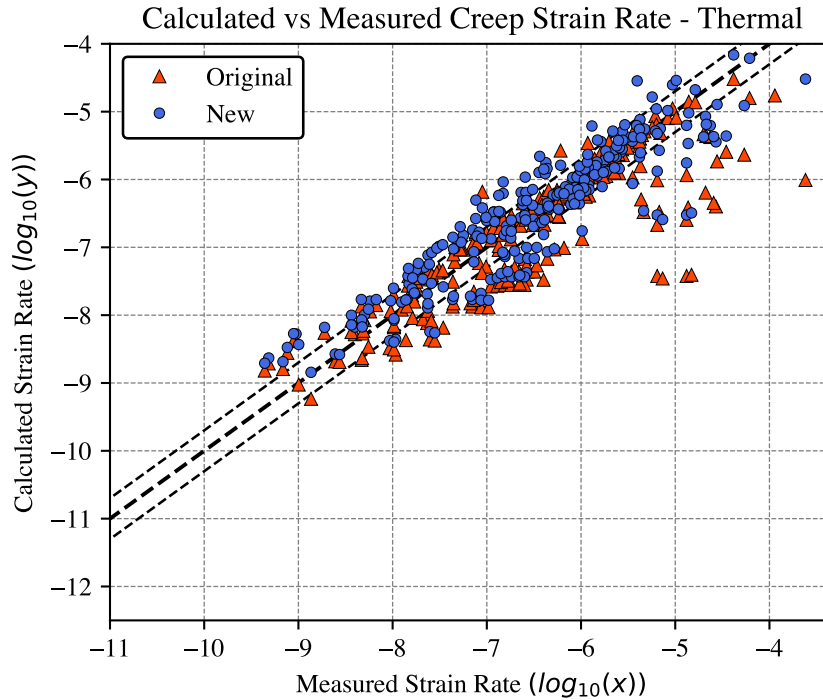
Fig. 10. Measured vs. calculated creep strain rates from using the original MATPRO expression (original) and the updated stoichiometry and thermal creep parameters (new).

Finally, the fission-dependent terms were refit. As previously mentioned, the fission-induced creep term was changed from an Arrhenius relation with temperature to an athermal linear relation to better

reflect the physical understanding of this mechanism. The resulting coefficient of this linear term was refit along with the fission rate prefactor in the sliding/diffusional creep term. The original and modified values for this refitting series are shown in Table IX. The A_2 parameter increased nearly $4\times$ the original value, while the A_7 parameter increased nearly $2\times$. This is consistent with values reported in literature for the athermal creep term and implies that the contribution of fission on the creep deformation is underrepresented in the original MATPRO model. The calculated vs. measured creep rate comparison for the original and modified model is shown in Figure 11. In this figure, because the modified model shown in Equation 17 was used, the original values do not have as wide of a dispersion as illustrated in Figure 6. The modification of the fission-related contributions results in, as expected, a general increase in calculated creep rates for all data with irradiation. Again, this fitting series shows an improvement to the RMSE and R^2 values shown in Table X.

TABLE IX. Original and refitted irradiation creep parameters.

| Model Parameter	Original Value	Refit Value	Units
A_2	$1.31e\text{-}19$	$4.90e\text{-}19$	$\mu m^2\text{-}m^3\text{-}Pa^{-1}$
A_7	$7.78e\text{-}37$	$1.49e\text{-}36$	Dimensionless
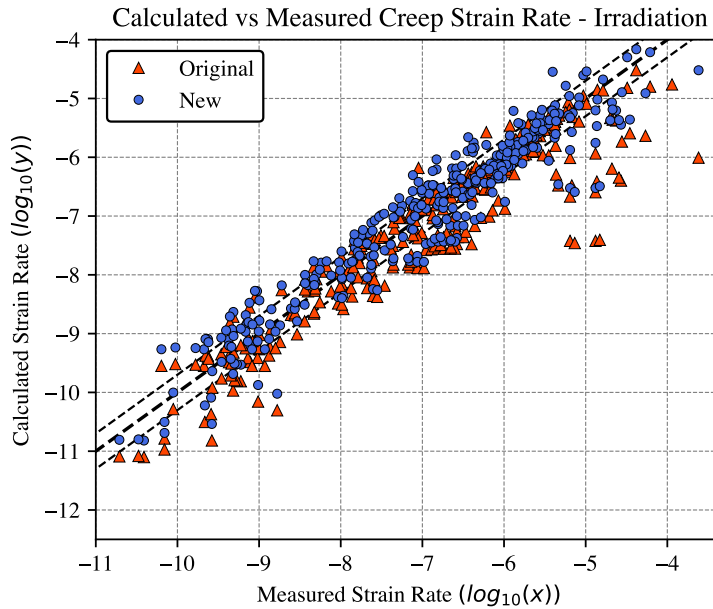
Fig. 11. Measured vs. calculated creep strain rates from using the original MATPRO expression (original) and the updated stoichiometry, thermal creep, and irradiation creep parameters (new).

The RMSE and R^2 values for the original model and each fitting series are shown in Table X. Because the fitting method used the logarithm (base 10) of creep rate, the RMSE of this value reports orders of magnitude. Therefore, the RMSE of the original indicates calculated values vary from the measured creep rates by nearly $3.7\times$, while the final series of fitting only varies by $2.6\times$. Future optimization of this

model may be performed using different model forms or statistical approaches, but for now, this model shows a good enough improvement over the original model to be implemented and tested in BISON.

TABLE X. RMSE and R^2 values from the fitting process.

Parameter Fit	RMSE	R^2
Original	0.57707	0.76003
Stoichiometry coefficients	0.48199	0.80784
Thermal coefficients	0.43556	0.84302
Irradiation coefficients	0.42129	0.91617

The individual creep data sets were revisited using this updated model, as shown in Figure 12. As expected, this plot shows a reduced spread of calculated creep rates compared to the original model (Figure 6). In particular, there is a substantial improvement in irradiated measurements from Solomon et al. (1971) and the thermal creep measurements from Burton and Reynolds (1973).
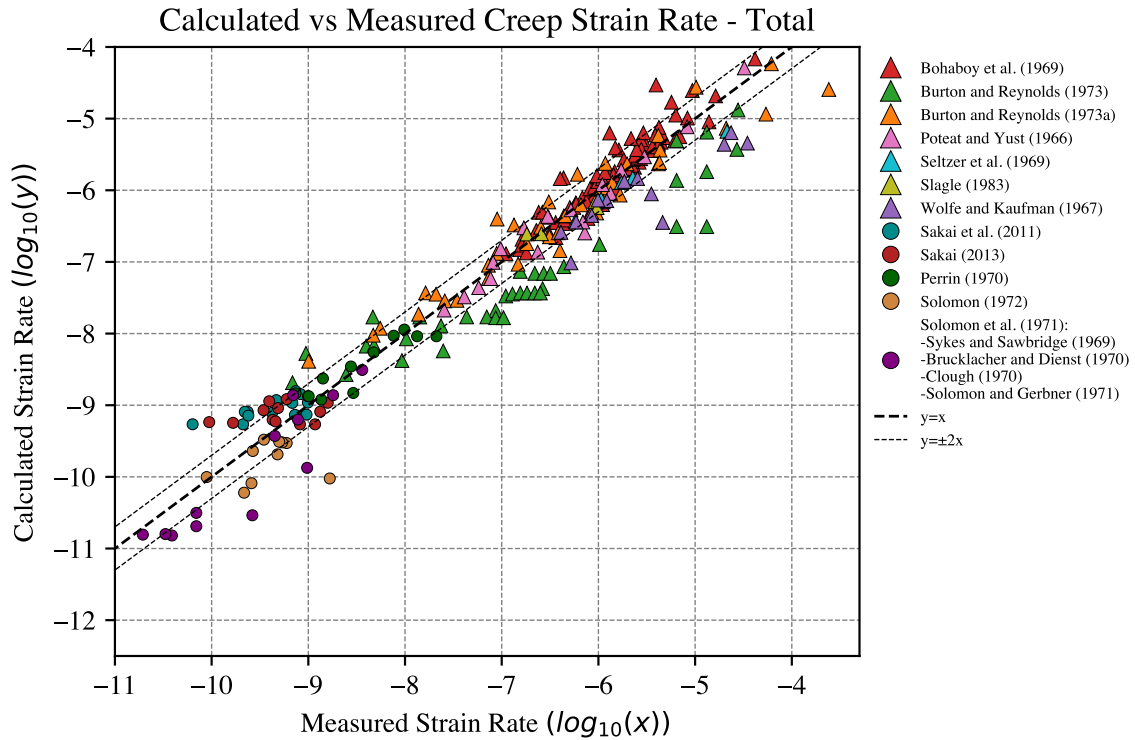
Fig. 12. Measured vs. calculated creep strain rates from various fuel creep experiments using the updated coefficients for the MATPRO expression. Triangle markers indicate thermal creep only, circle markers indicate irradiation.

A comparison of the original and modified creep rates delineated by contribution is shown in Figure 13. This plot shows the calculated strain rate produced from this effort (new) using solid lines and the current model implemented in BISON (using the athermal fission-induced creep term) using dashed lines.

For this illustration, the assumed conditions are a theoretical density of 98%, an applied stress of 75 MPa, a grain size of 25 μm, an oxide-to-metal ratio of 2.00, and a fission rate of 1E19 #/m^3-s.

The thermal creep contribution, shown in blue, shows a small increase using the modified model. The slight increase in the Q_2 activation energy (nearly the same for stoichiometric UO_2) shows nearly no effect (which would be apparent by the distance between the blue curves), indicating that the stress and prefactor changes are the most substantial. For the grain boundary sliding and diffusional creep mechanism, there is only a moderate increase in the creep rate nearly constant with temperature. The fission-induced creep shows a small increase corresponding to the 2× increase in the prefactor.
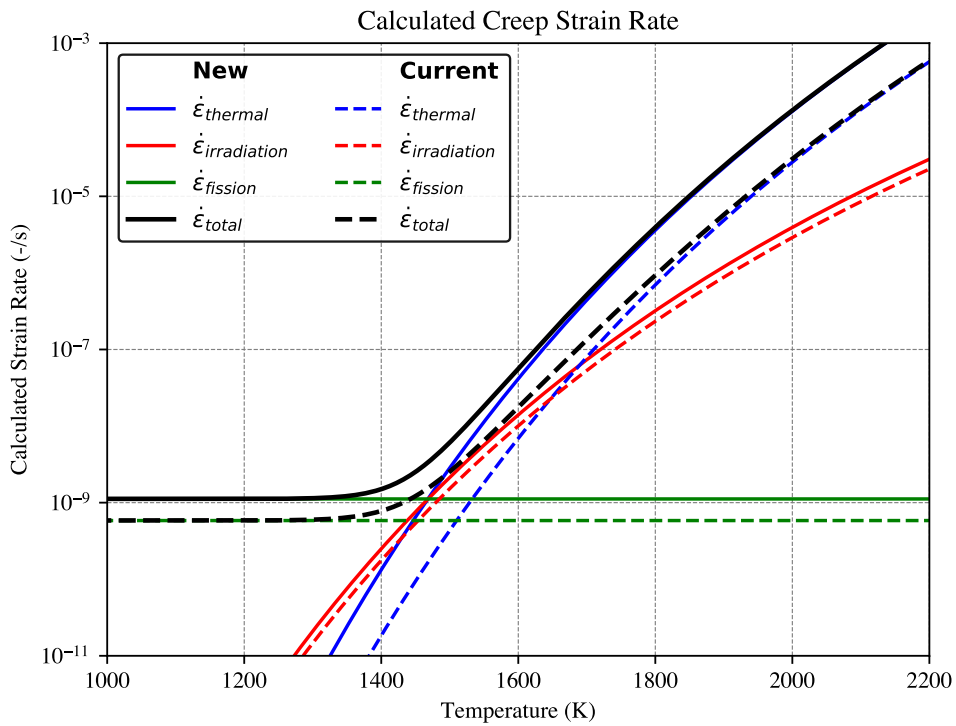
Fig. 13. Comparison of updated (new) and original (current) fuel creep model under selected conditions. This comparison shows the calculated strain rate with temperature using a density of 98%, a stress of 75 MPa, a grain size of 25 μm, an oxide-to-metal ratio of 2.00, and a fission rate of 1E19 #/m^3-s. Individual contributions to the creep strain are delineated by color.

This model has been implemented into BISON as an alternative to the original creep rate calculation. This new model option also incorporates several tests analogous to the original implementation. Future work for this model includes small optimizations to parameters and substantial testing across assessment cases.

B. Doped UO_2 creep rate surrogate model

Based on lower length-scale data provided by NEAMS collaborators at Los Alamos National Laboratory, a surrogate model for the diffusional creep rate $\dot{\varepsilon}_d$ (Equation 21) of doped UO_2 was developed. Parameters of the functional form are listed in Table XII.

$$\dot{\varepsilon}_d = \frac{42|\Omega|\pi\delta\sigma_v}{k_{B_J}TG^3} + D_{0_1}\exp\frac{-Q_1}{k_BT} \tag{21}$$

Details on the generation of the creep data are available in a separate report Galvin et al. (2023). The data was provided as 1,200,000 line table mapping from temperature, grain size, stress, and stoichiometry to a creep rate. The sampling of the input space is shown in Figure 14. Note that, while most input dimensions are sampled using a regular grid scheme, the stoichiometry exhibits a sparse irregular pattern.

Term	Description	Value
Ω	Atomic volume (m^3)	3.82×10^{-30}
D_{0_1}	Model (m^{2}s^{-1})	2.83×10^{-4}
Q_1	Model (eV)	3.63
k_B	Boltzmann constant (eV)	8.62×10^{-5}
k_{B_J}	Boltzmann constant (J)	1.38×10^{-23}
G	Grain size (m)	Input
δ	GB thickness (m)	Input
T	Temperature (K)	Input
σ_v	Stress (Pa)	Input

TABLE XII. Parameters for analytical description predicting diffusional creep rates.

To build and train the ROM, we used the PyTorch machine learning frameworkPaszke et al. (2019) within a Jupyter Kluyver et al. (2016) notebook. As a basis for the ROM a feed forward artificial neural network (ANN). The network features two hidden layers with 12 nodes each, an input layer with four nodes (corresponding to temperature, grain size, stress, and stoichiometry), and an output layer with one node (the creep rate). Sigmoid activation functions are applied on every layer except for the output layer, and all neighboring layers are fully connected. To prepare the training data set, we shuffled the provided data table, selected 60% of the lines randomly, and normalized each column by subtracting the column mean and dividing by the column standard deviation. As the creep rates span about 13 orders of magnitude, we decided to train the ROM on the logarithm of the creep rate, which we also normalized like the input columns.

For training, we utilized the PyTorch library, using a mean squared error loss function (`MSELoss`) and an Adam optimizer Kingma and Ba (2017). A mini batch approach with a batch size of 100,000 and 1,000,000 epochs was used to train the model using a graphics processing unit (GPU). Figure 15 shows a plot of the loss function over the ROM training process.

We analyze the quality of the trained surrogate by computing the root-mean-square (RMS) relative error of the predicted creep value over the test data set (all data point that were *not* used in the training process of the neural network). The RMS relative error for the test data set comes out as $\pm 3.74\%$, which agrees with the RMS relative error for the training data, indicating that no overfitting has occurred.

To identify the regions of high relative prediction error, we plot two-dimensional histograms with the relative error on the vertical axis and each of the four input dimensions on the horizontal axis in Figure
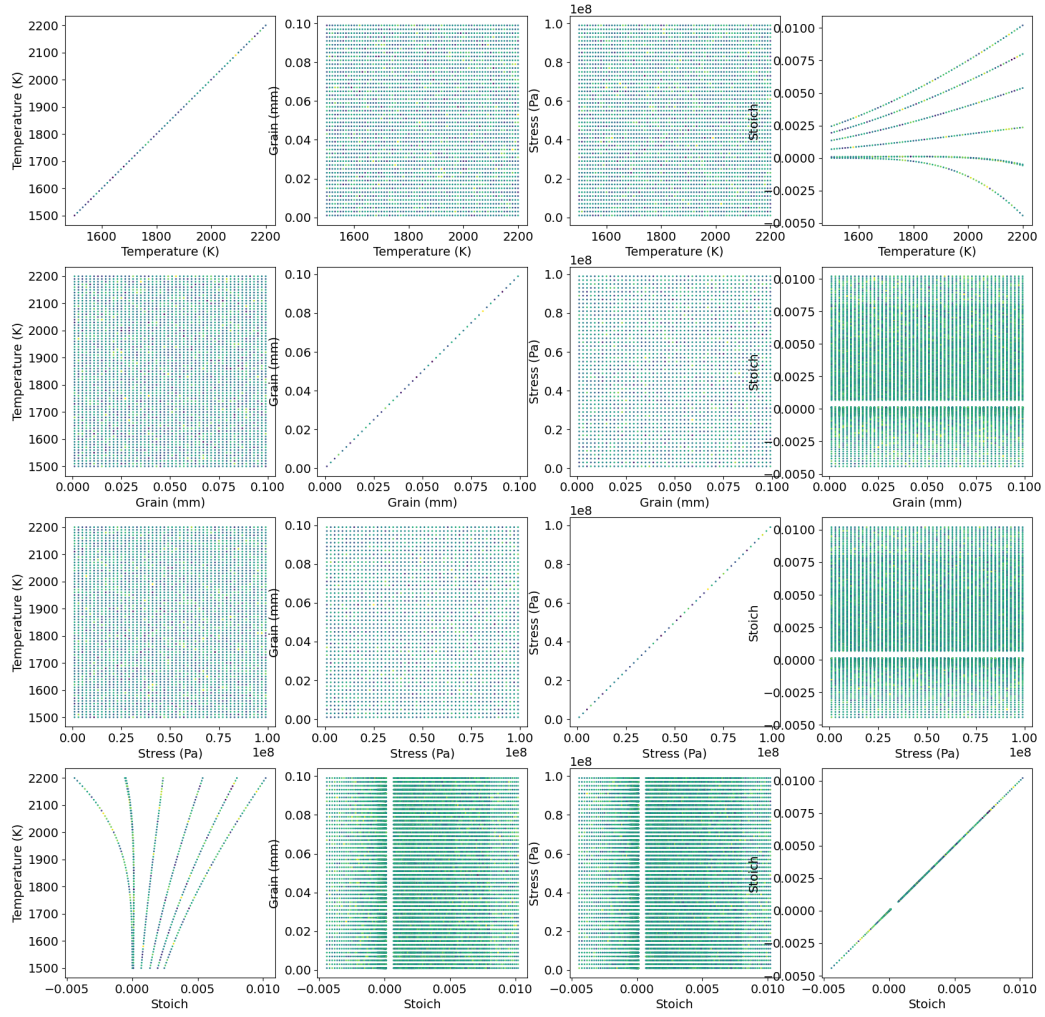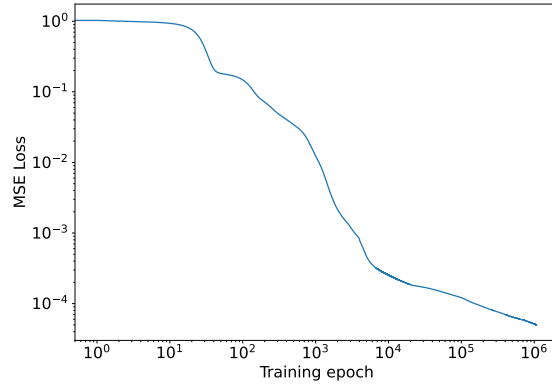
Fig. 14. Input space.

Fig. 15. Plot of the loss function, computed as the mean squared error (squared L2 norm) between each data point and the corresponding model prediction, over the training process (epochs) of the feed forward neural network surrogate model.

16. The color indicates the number of data points in each bin. We note that the errors are concentrated around zero in post regions, except low stresses (where the absolute error will be small) and very small grain sizes. The plot on the bottom right with stoichiometry on the horizontal axis shows a majority of data points located near or slightly above a stoichiometry value of zero.

Figure 17 shows a plot of the model creep rate prediction as blue lines against the training data (left) and testing data (right) as orange lines. The plotted data points were sorted by creep rate. The model shows satisfactory predictions over a very large range of creep rates. A logarithmic histogram of all relative errors of the predicted creep rates over both the training set (blue) and test data set (orange) is plotted in Figure 18. The similarity of the relative error distribution in training and test data indicates a robust fit of the surrogate model. Errors are peaked exponentially around zero.

We implemented the surrogate model in BISON as return mapping material class using two different approaches. The first approach uses the Multiphysics Object-Oriented Simulation Environment (MOOSE) LibTorch bindings to load the surrogate model, which was exported as a PyTorch model file from Python. We used autograd, the built-in automatic differentiation module in PyTorch to compute the derivative of the creep rate with respect to the applied stress. The performance of this approach was not optimal, firstly because the stock LibTorch implementation in MOOSE at that point lacked GPU support and secondly because derivatives with respect to the other three input values were computed but never used.

As an alternate approach, we used a native C++ implementation of an ANN developed in the Magpie code (Schwen and Schunert (2018)). We removed derivative calculation altogether, which required the switch from a Newton-Raphson return mapping solve to a secant solver. We found the performance of the derivative-free secant solve to be at least on par with the Newton-Raphson solve and, in the case of evaluating the surrogate, substantially higher than that of the LibTorch-based model with derivative calculation. The secant solver is under review as a pull request to to the MOOSE framework at the time of writing of this report.

Future work will include implementation of the surrogate model in the fully GPU-based NEML2 framework (Messner et al. (2023)) and retraining a surrogate to predict creep increments directly without
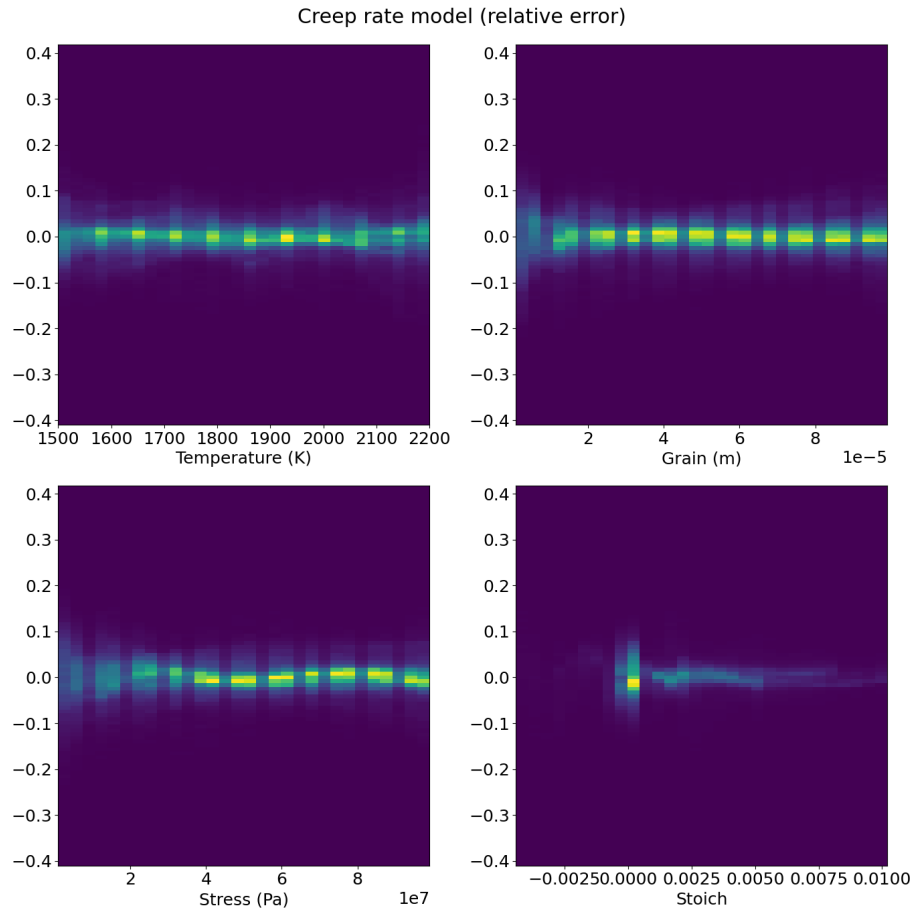
Fig. 16. Distribution of the the relative error (y-axis) of the model prediction as a density histogram, plotted against the four input dimensions of the surrogate.

performing return mapping. Bot tasks should lead to model performance increases.
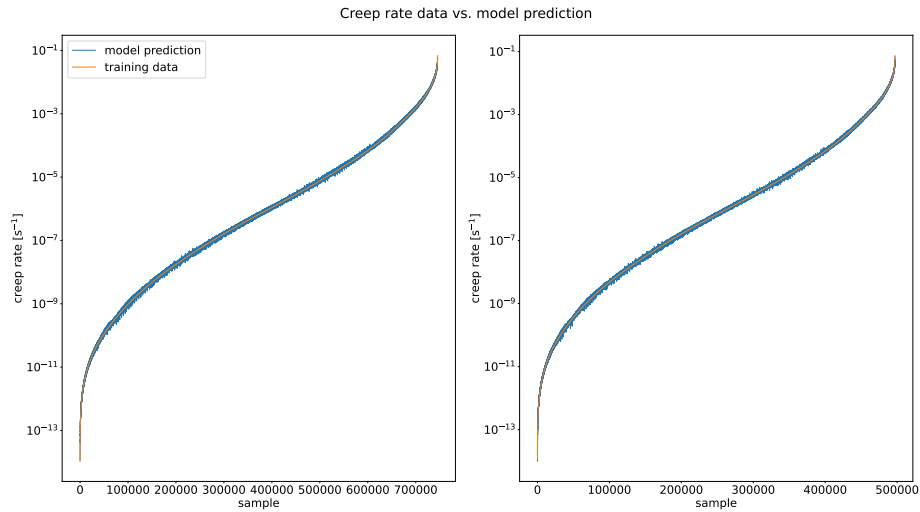
Fig. 17. Plot of the model creep rate prediction (blue lines) against the training data (left) and testing data (right) (orange lines). To generate the plot, the sample data was sorted by creep rate.
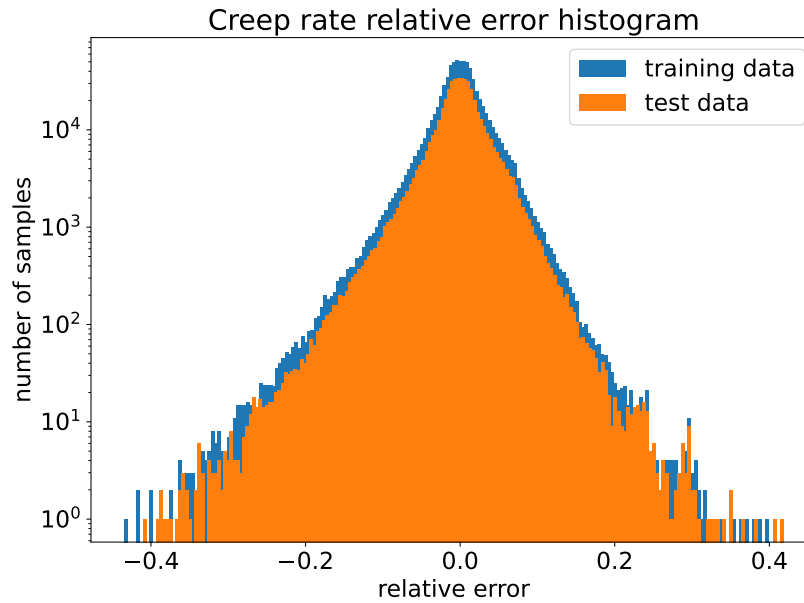

Fig. 18. Histogram of the relative errors of the predicted creep rates for the training data set (blue) and test data (orange). The histogram is sharply peaked with an RMS relative error of 3.74% in both the training and testing data, indicating that no overfitting has occurred.

IV. CONCLUSION

The work presented here expands BISON's modeling capabilities for doped and undoped UO_2 fuels. Specifically, the work presented here provides a commentary for improvements to calculating the spatial burnup distribution used for LWR fuels and implementing additional creep capabilities. These efforts mainly focused on enhancing BISON's modeling capabilities for these fuels to provide an improved prediction of the fuel thermomechanical behavior. These improvements include:

- Improved spatial calculation of burnup
- Implemented cross-sections for gadolinium for radial power distribution
- Modified UO_2 fuel creep model to better agree with experimental data
- Used ANN to develop and implement a surrogate creep model for Cr-doped fuel.

As an ongoing effort to improve the simulation capabilities of doped fuels for LWRs, these and other models will continue to be improved.

CM Allison, GA Berna, R Chambers, EW Coryell, KL Davis, DL Hagrman, DT Hagrman, NL Hampton, JK Hohorst, RE Mason, et al. Scdap/relap5/mod3. 1 code manual, volume iv: Matpro–a library of materials properties for light-water-reactor accident analysis. *DT Hagrman, NUREG/CR-6150, EGG-2720*, 4:4–234, 1993.

PE Bohaboy, RR Asamoto, and AE Conti. Compressive creep characteristics of stoichiometric uranium dioxide. Technical report, General Electric Co., Sunnyvale, Calif. Breeder Reactor Development Operation, 1969.

D Brucklacher, W Dienst, and F Thümmler. Investigation of the creep of ceramic nuclear fuels under neutron irradiation. Technical report, Kernforschungszentrum, Karlsruhe, Ger., 1970.

B Burton and GL Reynolds. The influence of deviations from stoichiometric composition on the diffusional creep of uranium dioxide. *Acta Metallurgica*, 21(12):1641–1647, 1973.

B Burton, GL Reynolds, and JP Barnes. The influence of grain size on the creep of uranium dioxide. *Journal of Materials Science*, 8:1690–1694, 1973.

DJ Clough. Irradiation induced creep of ceramic fuels. Technical report, United Kingdom Atomic Energy Authority, Harwell, Eng., 1970.

C. O. T. Galvin, D. A. Andersson, R. Sweet, L. Capolungo, and M. W. D. Cooper. Diffusional creep in UO$_2$ informed by lower length scale simulations. Tech. Rep. LANL-23/, Materials Science and Technology Division, Los Alamos National Laboratory (LANL), Los Alamos, NM United States, 9 2023.

JD Hales, SR Novascone, BW Spencer, RL Williamson, G Pastore, and DM Perez. Verification of the bison fuel performance code. *Annals of Nuclear Energy*, 71:81–90, 2014.

IAEA. Fuel Modelling at Extened Burnup (FUMEX-II): Report of a Coordinated Research Project 2002-2007. Technical Report IAEA-TECDOC-1687, International Atomic Energy Agency, 2002-2007.

J-C Kim. Physics calculations for IFA-681.1. Technical Report CP note 03-51, OECD Halden Reactor Project, 2003.

Diederik P. Kingma and Jimmy Ba. Adam: A method for stochastic optimization, 2017.

Thomas Kluyver, Benjamin Ragan-Kelley, Fernando Pérez, Brian Granger, Matthias Bussonnier, Jonathan Frederic, Kyle Kelley, Jessica Hamrick, Jason Grout, Sylvain Corlay, Paul Ivanov, Damián Avila, Safia Abdalla, and Carol Willing. Jupyter notebooks – a publishing format for reproducible computational workflows. In F. Loizides and B. Schmidt, editors, *Positioning and Power in Academic Publishing: Players, Agents and Agendas*, pages 87 – 90. IOS Press, 2016.

Jianchun Liu, Gary A. Pope, and Kamy Sepehrnoori. A high-resolution finite-difference scheme for nonuniform grids. *Applied Mathematical Modeling*, 19(3):162–172, 1995. doi:https://doi.org/10.1016/0307-904X(94)00020-7.

Mark Messner, TIANCHEN HU, and US DOE NE-NEAMS. Neml2 - the new engineering material model library, version 2, 1 2023. URL https://www.osti.gov//servlets/purl/1961125.

Adam Paszke, Sam Gross, Francisco Massa, Adam Lerer, James Bradbury, Gregory Chanan, Trevor Killeen, Zeming Lin, Natalia Gimelshein, Luca Antiga, Alban Desmaison, Andreas Kopf, Edward Yang, Zachary DeVito, Martin Raison, Alykhan Tejani, Sasank Chilamkurthy, Benoit Steiner, Lu Fang, Junjie Bai, and Soumith Chintala. Pytorch: An imperative style, high-performance deep learning library. In *Advances in Neural Information Processing Sys-*

tems 32, pages 8024–8035. Curran Associates, Inc., 2019. URL http://papers.neurips.cc/paper/9015-pytorch-an-imperative-style-high-performance-deep-learning-library.pdf.

JS Perrin. Irradiation-induced creep of uranium dioxide. *Journal of Nuclear Materials*, 39(2):175–182, 1971.

LE Poteat and CS Yust. Grain boundary reactions during deformation. Technical report, Oak Ridge National Lab., Tenn., 1966.

S. A. Press, W. H.and Teukolsky and B. P. Vetterling, W. T.and Flannery. *Numerical Recipes: The Art of Scientific Computing*. Cambridge University Press. New York, 3rd edition, 2007.

K Sakai. The fuel creep test ifa-701: results after four irradiation cycles. *vol. HWR-1039*, 2013.

K Sakai, H Hanakawa, and T Tverberg. Investigation of fission induced creep of uo2 and cr-doped fuel in ifa-701. Technical report, Technical Report HWR-1006, OECD Halden Reactor Project, 2011.

D. Schwen and S. Schunert. Magpie - mesoscale atomistic glue program for integrated execution. https://github.com/idaholab/magpie, 2018.

OD Slagle. Deformation behavior of uo2 above 2000° c. *Journal of the American Ceramic Society*, 67 (3):169–173, 1984.

A. Soba and A. Denis. Personal communication, 2017.

A. Soba, A. Denis, L. Romero, E. Villarino, and F. Sardella. A high burnup model developed for the DIONISIO code. *Journal of Nuclear Materials*, 433:160–166, 2013. doi:10.1016/j.jnucmat.2012.08.016.

A. Soba, M. Lemes, M.E. Gonznález, A. Denis, and L. Romero. Simulation of the behaviour of nuclear fuel under high burnup conditions. *Annals of Nuclear Energy*, 70, 2014. doi:10.1016/j.anucene.2014.03.004.

AA Solomon and RH Gebner. Instrumented capsule for measuring fission-induced creep of oxide fuels. *Nuclear Technology*, 13(2):177–184, 1972.

AA Solomon, Jules L Routbort, and JC Voglewede. *Fission-Induced Creep of UO2 and Its Significance to Fuel-Element Performance*. Argonne National Laboratory, 1971.

R J Stammler. Helios documentation. Technical report, FMS Fuel Management System, Studsvik Scandpower, Norway, 2000.

EC Sykes and PT Sawbridge. Irradiation creep of uranium dioxide. Technical report, Central Electricity Generating Board, Berkeley (England). Berkeley Nuclear Labs., 1969.

RA Wolfe and SF Kaufman. Mechanical properties of oxide fuels (lsbr/lwb development program). Technical report, Bettis Atomic Power Lab., Pittsburgh, Pa.(US), 1967.